Wireless Power Transfer

ARTICLE

Open Access

https://doi.org/10.48130/wpt-0025-0033

Wireless Power Transfer **2026**, 13: e003

Design and implementation of a high-frequency inverter with wide soft-switching range for dynamic wireless charging of electric vehicles

Ruiyan Wang, Youzheng Wang*, Pengyu Ding, Yingshuang He, Zijian Ma, Haoran Sun, Longnv Li, Gaojia Zhu and Yunhui Mei

School of Electrical Engineering, Tiangong University, Tianjin 300387, China

* Correspondence: youzhengwang@tiangong.edu.cn (Wang Y)

Abstract

To solve the problem that wireless power transfer (WPT) systems with multiple transmitters require more inverters and involve complex phase synchronization control between inverters, a dual-output zero-voltage switching (ZVS) inverter is proposed. It can generate two identical output voltages to realize synchronous driving of two transmitter coils, thereby reducing the number of inverters and switches required by the system, and simplifying system control. The output voltage gain characteristics of the inverter are analyzed and compared with those of existing typical inverters in WPT systems. The equivalent mathematical model of the system is constructed, and the output power characteristics are analyzed. Meanwhile, the operating states for soft-switching are analyzed and calculated. Theoretical analysis and experimental results indicate that the WPT system based on the proposed inverter can maintain high transmission efficiency during the movement of the receiver coil, with the maximum efficiency exceeding 90%.

Citation: Wang R, Wang Y, Ding P, He Y, Ma Z, et al. 2026. Design and implementation of a high-frequency inverter with wide soft-switching range for dynamic wireless charging of electric vehicles. *Wireless Power Transfer* 13: e003 https://doi.org/10.48130/wpt-0025-0033

Introduction

Wireless power transfer (WPT) is a technology that uses power electronics technology and modern control theory to achieve non-contact wireless transmission through soft media[1–3]. The World Economic Forum (WEF) has listed WPT as one of the top ten emerging technologies that have the greatest impact on the world and are most likely to provide answers to global challenges, for two consecutive years. It eliminates many problems associated with conventional contact power transmission methods, and solves the power supply problems of equipment in extreme, harsh, and complex environments (such as deep sea, deep space, flammable and explosive working environments). It meets people's requirements for safety, flexibility, and reliability of electrical equipment[4–7].

WPT technology is a research hotspot[8–10] due to its advantages of safety, convenience, flexibility, and freedom from structural and topological limitations[11,12]. In recent years, WPT technology has been gradually applied to mobile loads (such as wireless charging of electric vehicles, transport vehicles in logistics systems, transmission mechanisms in storage systems, and inspection robots in substations[13–15]), namely dynamic WPT systems. There are two common power supply modes shown in Figs. 1 and 2. Figure 1 illustrates the integrated single rail power supply mode[16,17]. When the electric equipment is driving above the transmitting rail, the receiver coil can obtain continuous energy. However, the disadvantage of the single-rail power supply mode is that the length of the energy transmitting rail is much larger than the size of the receiver coil, resulting in a small coupling coefficient and significant magnetic field exposure problems, making it unsuitable for long-distance applications. Figure 2 illustrates the power supply mode of the segmented rail (for ease of description, transmitting rails and transmitting coils are collectively referred to as transmitting rails subsequently). Multiple transmitting rails are laid in sequence on the moving path of the electric equipment, enabling segmented power supply of the mobile equipment and thus addressing the issues associated with the integrated single-rail power supply mode. In this power supply mode, there are two converter drive modes. In the single-converter drive mode shown in Fig. 2a[18], multiple transmitting rails share one converter, which can realize synchronous driving of multiple transmitting rails but requires an additional rail switching circuit to minimize losses from non-working rails. Simultaneously, this drive mode demands high converter capacity and has low system redundancy, making it not the optimal driving solution for long-distance applications. The multi-converter drive mode shown in Fig. 2b can achieve the independent control of each transmitting rail, with higher system redundancy, making it more suitable for long-distance applications[19]. However, this drive mode requires a large number of converters, increasing system cost, and maintenance complexity.

As a power converter for WPT systems, in addition to the commonly used bridge, push-pull and class-E inverters, reported topologies include matrix converters[20], multi-level inverters[21], three-phase inverters[22–24], and parallel multiple inverters[25], etc. Research on these topologies mainly focuses on enhancing system power. They all involve a larger number of switching devices or DC energy storage components, and most are single-output topologies, which are more suitable for driving a single transmitting rail. As an integrated single-stage boost inverter, the high step-up inverter can realize boost and conversion between direct current and alternating current at the same time. It has the characteristics of a few switching devices, which is a simple structure and control strategy. It is often used to isolate DC-DC power supplies, photovoltaic inverters, and induction heating[26,27].

This paper proposes a high-frequency inverter with dual-output and wide-range soft-switching characteristics for dynamic wireless charging of electric vehicles. Compared with the multi-converter

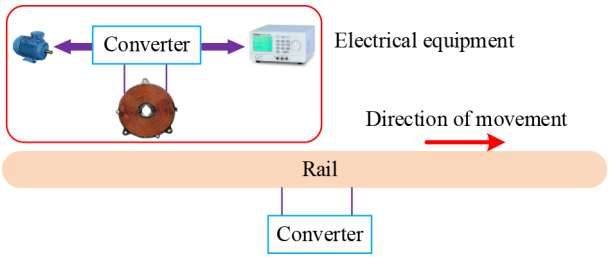

Fig. 1 Single rail power supply mode.

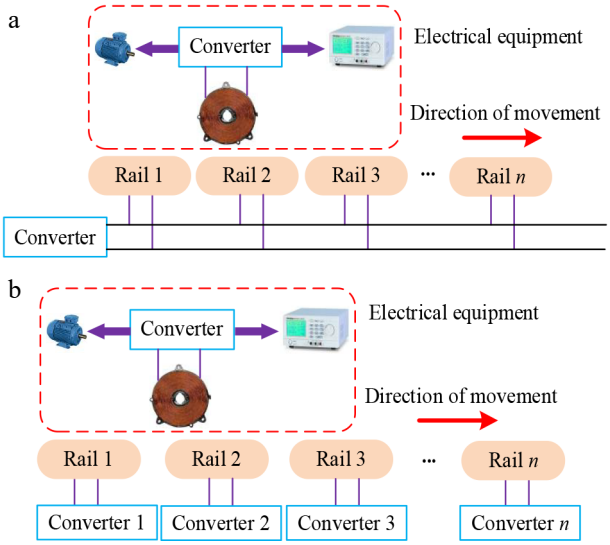

Fig. 2 Segmented rail (multi-coil array) supply mode. (a) Single converter power supply mode. (b) Multiple converter power supply mode.

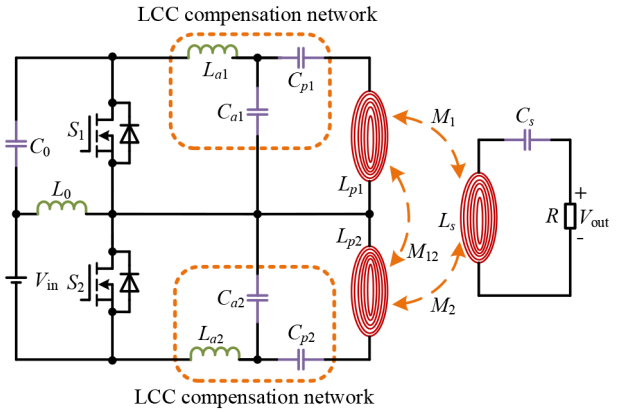

Fig. 3 Main circuit of the proposed dual-output inverter with wide soft-switching range for dynamic wireless charging of electric vehicles.

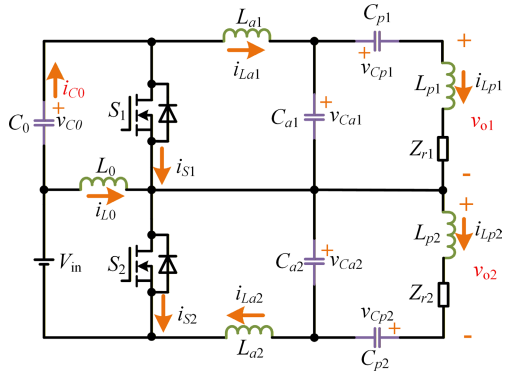

Fig. 4 Equivalent circuit of Fig. 3.

driving mode in Fig. 2b, the inverter can generate two identical outputs to drive two segments of transmitting rails, reducing the number of inverters and simplifying system control. On the other hand, compared with inverters commonly used in WPT systems, the proposed inverter can ensure the same voltage output capacity with fewer switching devices, further reducing the number of switching devices in a single inverter. It should be noted that the WPT system based on the proposed inverter is actually composed of multiple subsystems with the same structure and parameters, where each subsystem includes the proposed inverter and two segments of transmitting rails. The operation characteristics and rules of each subsystem are identical. This paper studies and analyzes a single subsystem, and the results are applicable to other subsystems, which can then be extended to the entire system.

Analysis of topology and operating mode

Circuit structure of the dual-output inverter

The topology of the proposed dual-output ZVS inverter for WPT systems is illustrated in Fig. 3. Figure 4 is the equivalent circuit diagram of Fig. 3. In Fig. 4, the direction of each current indicated by the orange arrow is the positive reference direction, and the terminal of each voltage symbol '+' is the positive reference terminal. The dual-output inverter consists of two switches S_1, S_2, inductor L_0, and capacitor C_0. LCC resonant compensation network with constant current output characteristics is adopted at the energy transmitter, composed of compensation capacitors C_{a1}, C_{a2}, C_{p1}, C_{p2}, and compensation inductors L_{a1} and L_{a2}. L_s denotes the receiver coil, C_s denotes the series resonant compensation capacitor, and R is the equivalent load resistance of the system. M_{12} denotes the cross mutual inductance between L_{p1} and L_{p2}; M_1 and M_2 are the mutual inductance between L_s and L_{p1}, L_{p2} respectively. V_{in} and I_{in} denote the input voltage and current of the inverter respectively. i_{S1} and i_{S2} denote the currents flowing through S_1 and S_2 respectively. i_{C0} and i_{L0} denote the current of C_0 and L_0 respectively, and v_{C0} denotes the voltage across C_0. Z_{r1} and Z_{r2} are the equivalent reflection impedances of the two transmitter coils.

Operating principle

To analyze the operating principle of the proposed inverter, the following assumptions are made: (1) Inductors and capacitors are ideal components with no internal resistance, and C_0 is sufficiently large to maintain a constant voltage across its terminals; (2) The internal resistance and voltage drop of all switches are equal to zero; (3) The parameters of each energy transmitter are symmetrical. The relevant parameters can be expressed as follows:

$$\begin{cases} L_{a1} = L_{a2} = L_a \\ C_{a1} = C_{a2} = C_a \\ C_{p1} = C_{p2} = C_p \\ L_{p1} = L_{p2} = L_p \end{cases} \tag{1}$$

Considering the influence of cross-mutual inductance, the expressions of the system resonant angular frequency ω_0 and resonant frequency f_0 are as follows:

$$\omega_0 = 2\pi f_0 = \frac{1}{\sqrt{L_a C_a}} = \frac{1}{\sqrt{\left(L_p + M_{12} - L_a\right) C_p}} = \frac{1}{\sqrt{L_s C_s}} \tag{2}$$

where, f_S denotes the switching frequency of the proposed inverter and f_0 denotes the resonant frequency of the system.

When f_S is equal to f_0, the key operating waveforms of the inverter are illustrated in Fig. 5, where T and D are the operating period and duty cycle of the inverter, respectively. t_d denotes the dead zone to prevent the bridge arm from passing through; V_B is the amplitude of the inverter's input voltage. The expression defining V_B is:

$$V_B = V_{C0} + V_{\text{in}} \tag{3}$$

The equivalent circuits of the inverter for various operating modes are illustrated in Fig. 6, where the directions marked by each arrow are the actual directions of each current at the initial instant of the mode. The proposed inverter has 11 operating modes in one operating cycle, and the analysis of each operating mode is as follows:

(1) Mode 1 (t_0~t_1): At t_0, S_2 is turned off. The current i_{S2} flowing through S_2 is commutated to S_1 and flows through its body diode, denoted as i_{S1}. Meanwhile, v_{o1} decreases to zero while v_{o2} increases to V_B. i_{C0} reverses polarity and C_0 enters charging state. In this mode, i_{L0} starts to decrease linearly from its maximum value.

(2) Mode 2 (t_1~t_2): At t_1, S_1 is turned on. When S_1 is turned on, the voltage stress across S_1 is zero, enabling S_1 to achieve ZVS turn-on. In this mode, i_{L0} continues to decrease linearly. Simultaneously, the condition for S_1 to achieve ZVS turn-on is derived as follows:

$$i_{S2}(t_0) > 0 \tag{4}$$

If Eq. (4) is not satisfied, when S_2 is turned off, u_{S2} is clamped to zero by its body diode, enabling ZVS turn-off of S_2.

(3) Mode 3 (t_2~t_3): At t_2, i_{La1} crosses zero in the reverse direction, and i_{La2} crosses zero in the forward direction; subsequently, i_{La1} starts to increase in the reverse direction, while i_{La2} starts to increase in the positive direction. In this mode, i_{L0} continues to decrease linearly.

(4) Mode 4 (t_3~t_4): At t_3, i_{S1} crosses zero in the positive direction, commutates from the body diode of S_1 to S_1 itself, and S_1 begins to conduct. In this mode, i_{L0} continues to decrease linearly.

(5) Mode 5 (t_4~t_5): At t_4, i_{C0} crosses zero in the reverse direction, and C_0 enters the state. In this mode, i_{L0} continues to decrease linearly.

(6) Mode 6 (t_5~t_6): At t_5, S_1 is turned off. i_{S1} is commutated to S_2 and flows through its body diode. v_{o2} drops to zero while v_{o1} rises to V_B. i_{C0} reverses polarity and C_0 enters a charging state. In this mode, i_{L0} starts to increase linearly from its minimum value.

(7) Mode 7 (t_6~t_7):At t_6, S_2 is turned off. Since the voltage stress across S_2 is zero at turn on, S_2 can achieve ZVS turn on. In this mode, i_{L0} continues to increase linearly. Meanwhile, the condition for S_2 to achieve ZVS turn-on is derived as follows:

$$i_{S1}(t_5) > 0 \tag{5}$$

If Eq. (5) is not satisfied, when S_1 is turned off, u_{S1} is clamped to zero by the body diode of S_1, enabling ZVS turn-off of S_1.

(8) Mode 8 (t_7~t_8): At t_7, i_{S2} crosses zero, i_{S2} transfers from the body diode of S_2 to S_2, and S_2 begins to conduct. In this mode, i_{L0} continues to rise linearly.

(9) Mode 9 (t_8~t_9): At t_8, i_{C0} and i_{La2} cross zero in the reverse direction, i_{La1} crosses zero in the forward direction, and C_0 enters a discharging state. In this mode, i_{L0} continues to increase linearly.

(10) Mode 10 (t_9~t_{10}): At t_9, i_{C0} and i_{La2} cross zero in the forward direction, i_{La1} crosses zero in the reverse direction, and C_0 enters a charging state. In this mode, i_{L0} continues to increase linearly.

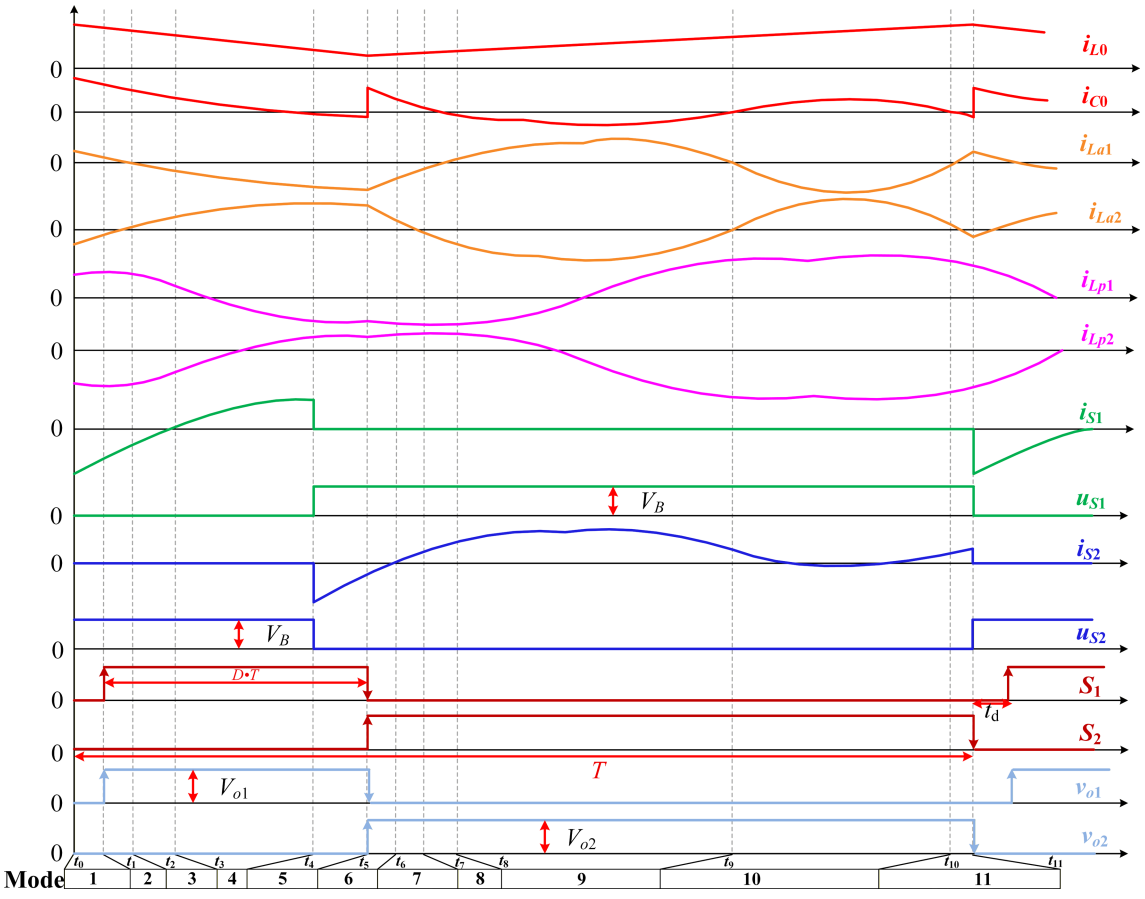

Fig. 5 Theoretical operating waveforms of key components.

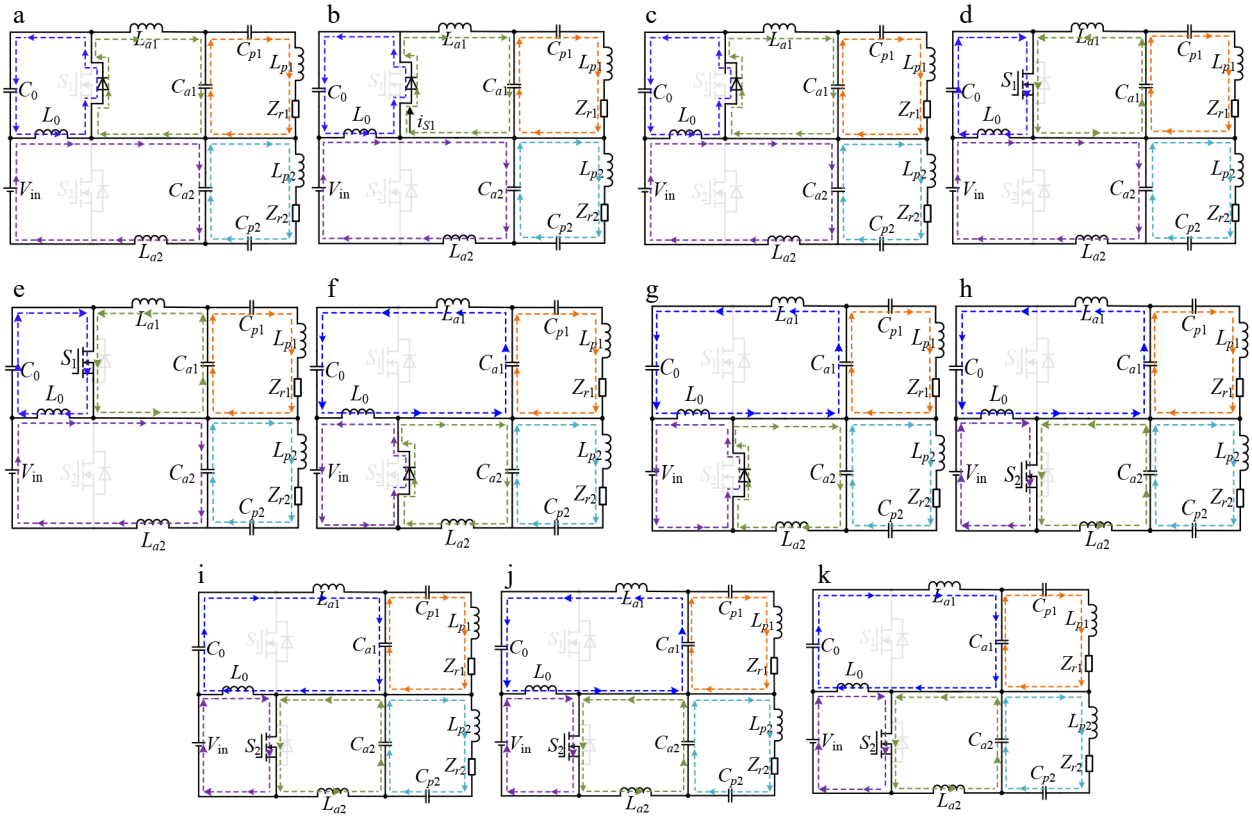

Fig. 6 Equivalent circuits in each of the operating modes. (a) Mode 1; (b) Mode 2; (c) Mode 3; (d) Mode 4; (e) Mode 5; (f) Mode 6; (g) Mode 7; (h) Mode 8; (i) Mode 9; (j) Mode 10; (k) Mode 11.

(11) Mode 11 (t_{10}~t_{11}): At t_{10}, i_{C0} and i_{La2} cross zero in the reverse direction again, i_{La1} crosses zero in the forward direction again, and C_0 enters a discharging state again. In this mode, i_{L0} continues to increase linearly. At t_{11}, S_2 is turned off and the inverter enters the next operating cycle.

Performance analysis

Analysis of voltage gain

With regard to Fig. 5, the dead time t_d is much smaller than the inverter's duty cycle T and can be ignored to simplify the analysis. Based on the operating principle of the dual-output inverter, the voltage expression across L_0 is derived as:

$$V_{L0} = \begin{cases} -V_{C0} & t_0 \leqslant t \leqslant t_5 \\ V_{\text{in}} & t_5 \leqslant t \leqslant T \end{cases} \tag{6}$$

In steady state, the volt-second balance theorem is applied to inductor L_0, leading to the following equation:

$$V_{\text{in}} DT = V_{C0}(1-D)T \tag{7}$$

Combining Eqs (3) and (7), the expressions for V_{C0} and V_B are derived as follows:

$$V_{C0} = \frac{DV_{\text{in}}}{1-D} \tag{8}$$

$$V_B = \frac{V_{\text{in}}}{1-D} \tag{9}$$

According to Fig. 5, the Fourier series expansions of the two output voltages v_{o1} and v_{o2} of the inverter are obtained by ignoring the dead time.

$$v_{o1} = DV_B - \frac{\sqrt{2}V_B}{\pi}\sum_{n=1}^{\infty}\left[\frac{\sqrt{1-\cos 2n\pi D}}{n}\sin(n\omega_0 t - \varphi_n)\right] \tag{10}$$

$$v_{o2} = (1-D)V_B + \frac{\sqrt{2}V_B}{\pi}\sum_{n=1}^{\infty}\left[\frac{\sqrt{1-\cos 2n\pi D}}{n}\sin(n\omega_0 t - \varphi_n)\right] \tag{11}$$

φ_n = arctan [cot ($n\pi D$)] denotes the phase of the nth harmonic of v_{o1} and v_{o2}.

The phasor expression for the RMS value of the nth harmonic of v_{o1} and v_{o2} is as follows:

$$\begin{cases} \dot{V}_{o1n} = V_{o1n}\angle\varphi_n = \dfrac{V_B\sqrt{1-\cos(2n\pi D)}}{n\pi}\angle(\pi-\varphi_n) \\ \dot{V}_{o2n} = V_{o2n}\angle\varphi_n = \dfrac{V_B\sqrt{1-\cos(2n\pi D)}}{n\pi}\angle-\varphi_n \end{cases} \tag{12}$$

It can be seen from Eq. (12) that the two output voltages of the dual-output inverter are equal in magnitude and opposite in direction. Since the LCC network has excellent filtering characteristics, the rail current approximates a sine wave, with energy primarily transmitted through the fundamental component. The inverter's output voltage gain is defined as:

$$M_{v-p} = \frac{|\dot{V}_{o1,1}|}{V_{\text{in}}} = \frac{|\dot{V}_{o2,1}|}{V_{\text{in}}} \tag{13}$$

where, $|\dot{V}_{o1,1}|$ and $|\dot{V}_{o2,1}|$ denote the phasor expression for the RMS value of the fundamental component of v_{o1} and v_{o2}, respectively.

The relationship between M_{v-p} and D is depicted in Fig. 7. In practical operation, when D = 1, i_{L0} will increase continuously, eventually resulting in excessive current through the inverter, which may lead to burnout. To ensure an adequate safety margin for the inverter, the range of D in Fig. 7 is set to 0~0.9. It can be seen from Fig. 7

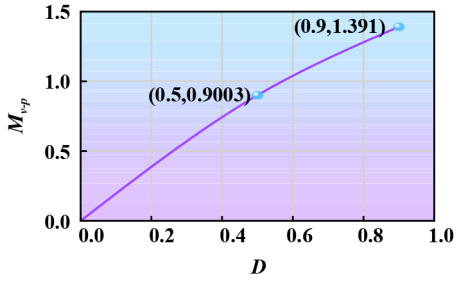

Fig. 7 The relationship between $M_{v\text{-}p}$ and D.

that $M_{v\text{-}p}$ is positively correlated with D, with $M_{v\text{-}p|D=0.5} = 0.9003$, and $M_{v\text{-}pmax} = 1.391$.

Comparative analysis

Table 1 compares the proposed dual-output inverter with existing common inverters in terms of output voltage gain range, number of input and output ports, and the number of switching devices. From Table 1, it is evident that the proposed dual-output inverter offers a wider voltage gain range compared to existing inverters. In terms of output quantity, all inverters except the three-phase inverter are single-output. However, the three-phase inverter requires three times as many switching devices as the proposed dual-output inverter, and there exists a phase difference between its phase outputs. Regarding the number of switching devices, both the voltage-type half-bridge inverter and the proposed dual-output inverter require only two switching devices. However, the voltage-type half-bridge inverter has a lower output voltage gain and fewer outputs compared to the proposed dual-output inverter. In summary, the proposed dual-output inverter can achieve more outputs and a wider voltage gain range with fewer switching devices, enabling synchronous driving of more transmitter coils.

Table 1. The comparison between the proposed dual output inverter and several typical inverters.

Type of inverter	Voltage gain	Number of input ports	Number of output ports	Number of switching devices
Voltage type half bridge inverter	0~0.45	1	1	2
Voltage type full bridge inverter	0~0.9	1	1	4
Matrix converter	0~0.64	1	1	8
Multi-level inverter	0~1.35	1	1	8
Three-phase inverter	0~0.78	1	3	6
The proposed inverter	0~1.39	1	2	2

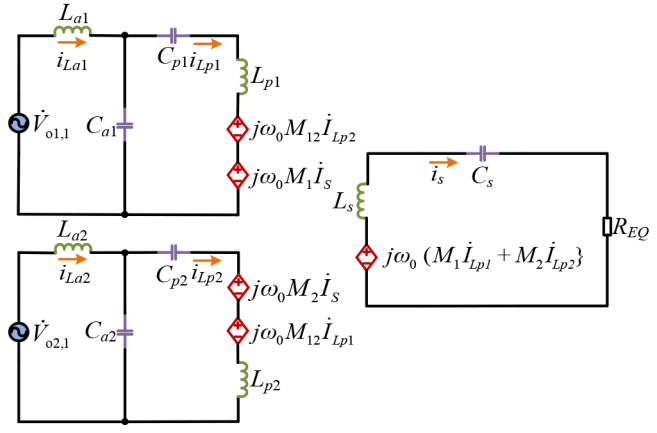

Fig. 8 The mutual inductance equivalent circuit in Fig. 3.

Output power analysis of the power system

Using the fundamental equivalence principle, Fig. 3 can be simplified to the equivalent circuit shown in Fig. 8. In Fig. 3, the phases of i_{La2} and i_{Lp2} are opposite to those of i_{La1} and i_{Lp1}. Thus, in practical applications, the connection direction of the inverter's second output network should be reversed to ensure that i_{La1} and i_{La2}, as well as i_{Lp1} and i_{Lp2}, are in phase, thereby avoiding power imbalance. Therefore, for ease of analysis in this section, i_{Lp1} and i_{Lp2} are reversed in phase.

Based on Kirchhoff's law of voltage (KVL), the relationship between system voltage and current is expressed as follows:

$$\begin{bmatrix} \dot{V}_{o1,1} \\ \dot{V}_{o2,1} \\ \dot{V}_{o1,1} \\ \dot{V}_{o2,1} \\ 0 \end{bmatrix} = \begin{bmatrix} Z_a & -1/j\omega_0 C_a & 0 & 0 & 0 \\ 0 & 0 & Z_a & -1/j\omega_0 C_a & 0 \\ j\omega_0 L_a & Z_p & 0 & 0 & -j\omega_0 M_1 \\ 0 & 0 & j\omega_0 L_a & Z_p & -j\omega_0 M_2 \\ 0 & j\omega_0 M_1 & 0 & j\omega_0 M_2 & -Z_s - R \end{bmatrix} \begin{bmatrix} \dot{I}_{La1} \\ \dot{I}_{Lp1} \\ \dot{I}_{La2} \\ \dot{I}_{Lp2} \\ \dot{I}_s \end{bmatrix} \tag{14}$$

where, $\begin{cases} Z_a = j\omega_0 L_a + \dfrac{1}{j\omega_0 C_a} \\ Z_p = j\omega_0 \left(L_p + M_{12}\right) + \dfrac{1}{j\omega_0 C_p} \\ Z_s = j\omega_0 L_s + \dfrac{1}{j\omega_0 C_s} \end{cases}$.

By substituting Eqs (2) and (14) into Eq. (13), the expression of current in each branch of the system can be obtained as:

$$\begin{cases} \dot{I}_{L1} = \dfrac{\dot{V}_{o1,1} M_1 (M_1 + M_2)}{{L_a}^2 R} \\ \dot{I}_{L2} = \dfrac{\dot{V}_{o1,1} M_2 (M_1 + M_2)}{{L_a}^2 R} \\ \dot{I}_{p1} = \dfrac{\dot{V}_{o1,1}}{j\omega_0 L_a} \\ \dot{I}_{p2} = \dfrac{\dot{V}_{o1,1}}{j\omega_0 L_a} \\ \dot{I}_s = \dfrac{\dot{V}_{o1,1} (M_1 + M_2)}{L_a R} \end{cases} \tag{15}$$

From Eq. (15), it can be observed that $\dot{I}_{p1}$and $\dot{I}_{p2}$ are equal in magnitude and phase, and are independent of R, M_1, and M_2. Thus, two high-frequency currents with the same phase and magnitude can be generated in the two transmitting coils, avoiding complicated phase synchronization control. Based on Eq. (15), the system output power expression is further derived as:

$$P_{out} = \left|\dot{I}_s\right|^2 \cdot R = \frac{V_{o1,1}^2 (M_1 + M_2)^2}{{L_a}^2 R} \tag{16}$$

Using the parameters in Table 2 as the main parameters, the system output power characteristic curves are depicted in Fig. 9. Figure 9a illustrates the relationship between output power P_{out}, duty cycle D and mutual inductance $M_1 + M_2$. It can be seen that in the resonance state, P_{out} is positively correlated with D and $M_1 + M_2$.

Table 2. Main system parameters.

Parameter	Value	Parameter	Value
V_{in}	100 V	L_a	50 μF
L_p	100 μH	C_a	70.12 nF
L_0	150 μH	C_p	62.94 nF
L_s	130 μH	R	5 Ω
C_0	100 μF	M_{12}	5.7 μH
C_s	26.97 nF	f_0	85 kHz

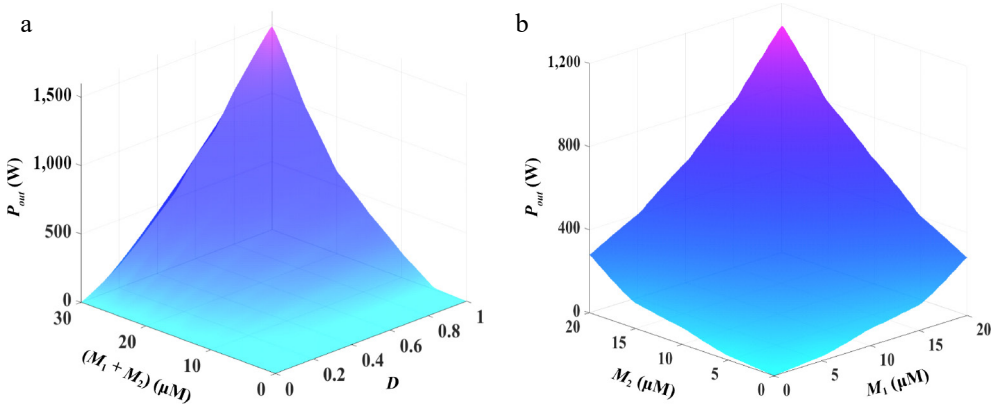

Fig. 9 The relationship among P_{out} with D, M_1, and M_2. (a) The relationship among P_{out} with D and $M_1 + M_2$. (b) The relationship among P_{out} with M_1 and M_2.

Figure 9b depicts the relationship between P_{out}, M_1, and M_2 at $D = 0.5$. It can be seen that P_{out} is positively correlated with M_1 and M_2, and the influence of M_1 and M_2 on P_{out} is symmetrical.

Operating conditions of soft-switching

According to Fig. 5, the voltage stress of S_1 and S_2 is:

$$v_{S1\max} = v_{S2\max} = V_B \tag{17}$$

The current stress on S_1 and S_2 is expressed as:

$$i_{S1\max} = i_{S2\max} = i_{S2}(t_0) \tag{18}$$

According to Figs. 5 and 6, the following expressions are derived:

$$i_{S1} = \begin{cases} i_{L2} - i_{L1} - i_{L0} & t_0 \leqslant t \leqslant t_5 \\ 0 & t_5 \leqslant t \leqslant t_{11} \end{cases} \tag{19}$$

$$i_{S2} = \begin{cases} 0 & t_0 \leqslant t \leqslant t_5 \\ i_{L0} + i_{L1} - i_{L2} & t_5 \leqslant t \leqslant t_{11} \end{cases} \tag{20}$$

According to Eqs (10) and (15), the fundamental wave time domain expressions of i_{La1} and i_{La2} are obtained as follows:

$$\begin{cases} i_{La1,1}(t) = \sqrt{2}\left|\dot{I}_{La1}\right|\sin(\omega_0 t + \pi - \phi_1) \\ i_{La2,1}(t) = \sqrt{2}\left|\dot{I}_{La2}\right|\sin(\omega_0 t - \phi_1) \end{cases} \tag{21}$$

where, $i_{La1,1}(t)$ and $i_{La2,1}(t)$ represent the fundamental components extracted from the Fourier series expansions of i_{La1} and i_{La2}, respectively.

To enhance analysis accuracy, it is necessary to calculate the higher harmonics of i_{La1} and i_{La2}. According to[28], the LCC network can be simplified as shown in Fig. 10 under high-order harmonics. It can be observed that high-order harmonics almost all the high-frequency current flows through L_a and C_a, while the transmitting coil circuit is equivalent to an open circuit. This explains why i_{La1} and i_{La2} exhibit high distortion,whereas i_{Lp1} and i_{Lp2} have high sinusoidality in Fig. 5.

According to Fig. 10, the impedance expression of LCC network under the nth harmonic is as follows:

$$Z_{1,n} = jn\omega_0 L_a + \frac{1}{jn\omega_0 C_a} = jZ_a\frac{n^2-1}{n} \tag{22}$$

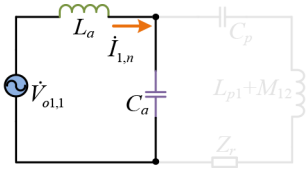

Fig. 10 Simplified model of LCC network under high order harmonics.

where, $Z_a = \omega_0 L_a = \sqrt{L_a/C_a}$, $n \geqslant 2$.

Hence, the nth harmonic expressions of i_{La1} and i_{La2} are obtained:

$$\begin{cases} i_{La1,n}(t) = \sqrt{2}\dfrac{\left|\dot{V}_{o1,n}\right|}{\left|Z_{1,n}\right|}\sin\left(n\omega_0 t - \phi_n + \dfrac{\pi}{2}\right) \\ i_{La2,n}(t) = \sqrt{2}\dfrac{\left|\dot{V}_{o2,n}\right|}{\left|Z_{1,n}\right|}\sin\left(n\omega_0 t - \phi_n + \dfrac{\pi}{2}\right) \end{cases} \tag{23}$$

Then the total expression of i_{La1} and i_{La2} is as follows:

$$\begin{cases} i_{La1}(t) = i_{La1,1}(t) + \sum\limits_{n=2}^{\infty} i_{La1,n}(t) \\ i_{La2}(t) = i_{La1,1}(t) + \sum\limits_{n=2}^{\infty} i_{La1,n}(t) \end{cases} \tag{24}$$

Assuming ideal system operation (with zero losses), the average value of the inverter input current i_{in} can be expressed using the law of energy conservation as:

$$i_{in} = i_{L0m} - i_{C0m} = \frac{P_{out}}{V_{in}} \tag{25}$$

where, i_{L0m} denotes the average value of i_{L0}, and i_{C0m} denotes the average value of i_{C0}. In steady state, the capacitor satisfies the ampere-second balance principle, that is $i_{C0m} = 0$, then Eq. (25) can be rewritten as:

$$i_{L0m} = \frac{P_{out}}{V_{in}} \tag{26}$$

When S_2 is turned on, i_{L0} increases linearly, so the fluctuating value expression of i_{L0} is as follow:

$$\Delta i_{L0} = \frac{V_{in}DT}{L_0} \tag{27}$$

The expressions of i_{S2} and i_{S1} when the switches turn on are as follows:

$$\begin{cases} i_{S2}(t_0) = i_{L0m} + \dfrac{\Delta i_L}{2} + i_{La1}(t_0) - i_{La2}(t_0) \\ i_{S1}(t_5) = i_{La2}(t_5) - i_{La1}(t_5) - i_{L0m} + \dfrac{\Delta i_L}{2} \end{cases} \tag{28}$$

According to Eq. (28), the current stress of the switching devices and the soft-switching operating states can be determined. Using the parameters in Table 2 as the main system parameters, the relationship between $i_{S2}(t_0)$ with D, M_1, and M_2 is depicted in Fig. 11a. Figure 11b is a cross-sectional view of Fig. 11a at $M_2 = 15$ μH. It can be observed that $i_{S2}(t_0)$ is always positive regardless of the values of M_1, M_2, and D, indicating that ZVS turn on of S_1 can be achieved at any position of the receiving coil. The larger M_1, M_2, and D, the greater $i_{S2}(t_0)$ and the lower the current stress on the switches. Figure 12 illustrates the relationship between $i_{S1}(t_5)$, D, M_1, and M_2. Figure 12a shows the influence of M_1 and M_2 values on $i_{S1}(t_5)$ under

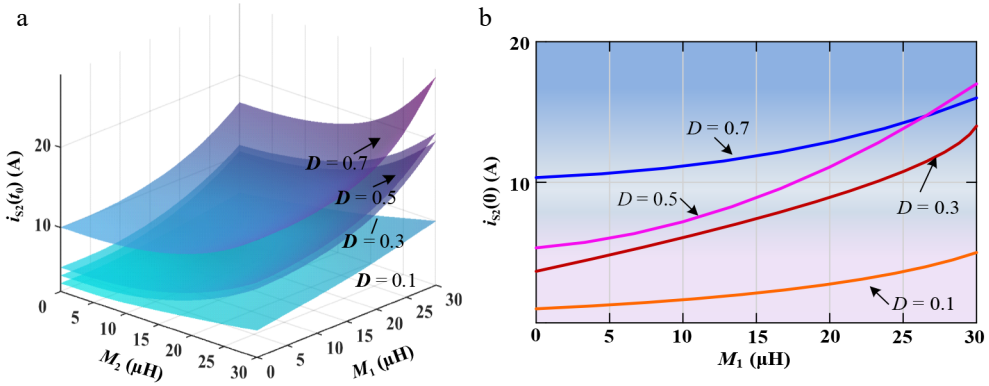

Fig. 11 The relationship among $i_{S2}(t_0)$ with D, M_1, and M_2. (a) The relationship among $i_{S2}(t_0)$ with D, M_1, and M_2 under different duty cycle conditions; (b) Cross-sectional view of (a) when M_2 = 15 μH.

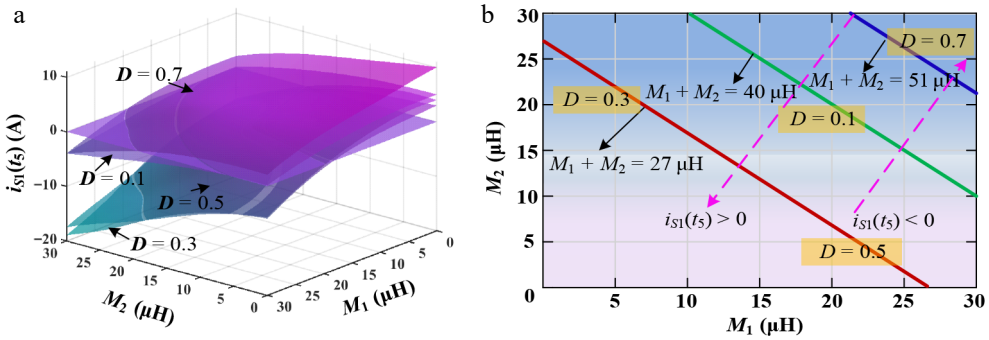

Fig. 12 The relationship among $i_{S1}(t_5)$ with D, M_1, and M_2. (a) The relationship among $i_{S1}(t_5)$ with D, M_1, and M_2 under different duty cycle conditions; (b) Polarity boundary line of $i_{S1}(t_5)$.

different duty cycles, while Fig. 12b presents the polarity boundary of $i_{S1}(t_5)$ in Fig. 12a. It can be observed that for a fixed duty cycle, the larger $M_1 + M_2$, the closer the receiving coil is to the center of the transmitting coil, the easier it is to achieve ZVS turn-off of S_1. Furthermore, the smaller $M_1 + M_2$, the closer the pick-up coil is to the edge of the transmitting coils, the easier it is to achieve ZVS turn-on of S_2. In any case, the inverter can always achieve two soft-switching states, which can reduce switching losses.

Experimental verification

Configuration of the experimental prototype

To verify the correctness of the theoretical analysis, and the feasibility and superiority of the proposed dual-output inverter, an experimental platform was built as shown in Fig. 13 according to the parameters in Table 2. The experimental setup consists of a DSP and FPGA controller, a dual-output inverter, a resonant compensation network, a coupling mechanism, and a load resistor. The DSP controller is used to generate drive signals for S_1 and S_2. The schematic diagram of the coupling mechanism is shown in Fig. 14a. The position x = 0 is defined as the receiver coil being centered between the two transmitter coils. The measured values of mutual inductances M_1, M_2, and M_{12} as functions of x are shown in Fig. 14b. It can be seen from Fig. 14b that M_1 and M_2 reach their maximum values at x = −7.5cm and x = 7.5 cm respectively. $M_1 + M_2$ is approximately symmetric with respect to x = 0, while M_{12} remains nearly constant.

Steady-state characteristic test

Figure 15 shows the experimental waveforms of the inverter output voltage and transmitting coil current at x = 0 and 7.5 cm, D = 0.3 and D = 0.7. It can be seen from Fig. 15 that when D = 0.3 and 0.7, the experimental values of V_B are 140 and 330 V, respectively. Meanwhile, the amplitudes and phases of i_{Lp1} and i_{Lp2} are essentially the same; the slight discrepancy arises primarily from the fact that the parameters of the two output resonant compensation networks of the inverter are not strictly consistent in practice. With the

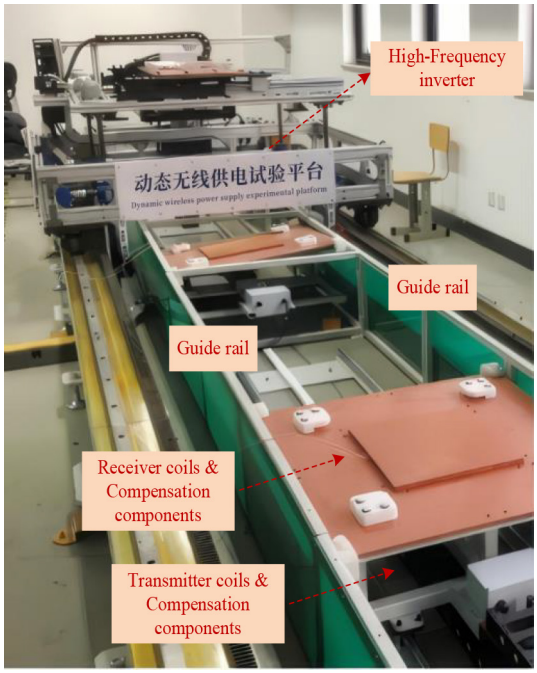

Fig. 13 Experimental platform.

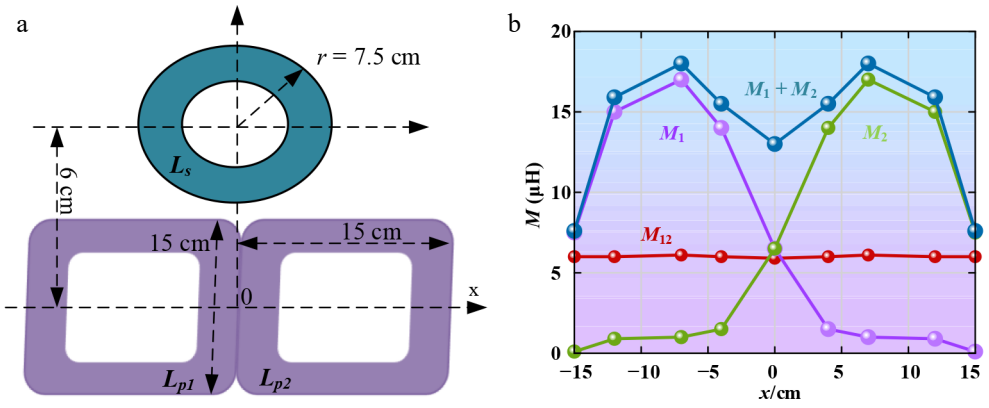

Fig. 14 The magnetic coupler. (a) Schematic diagram; (b) Measured mutual inductances vary with *x*-axis.

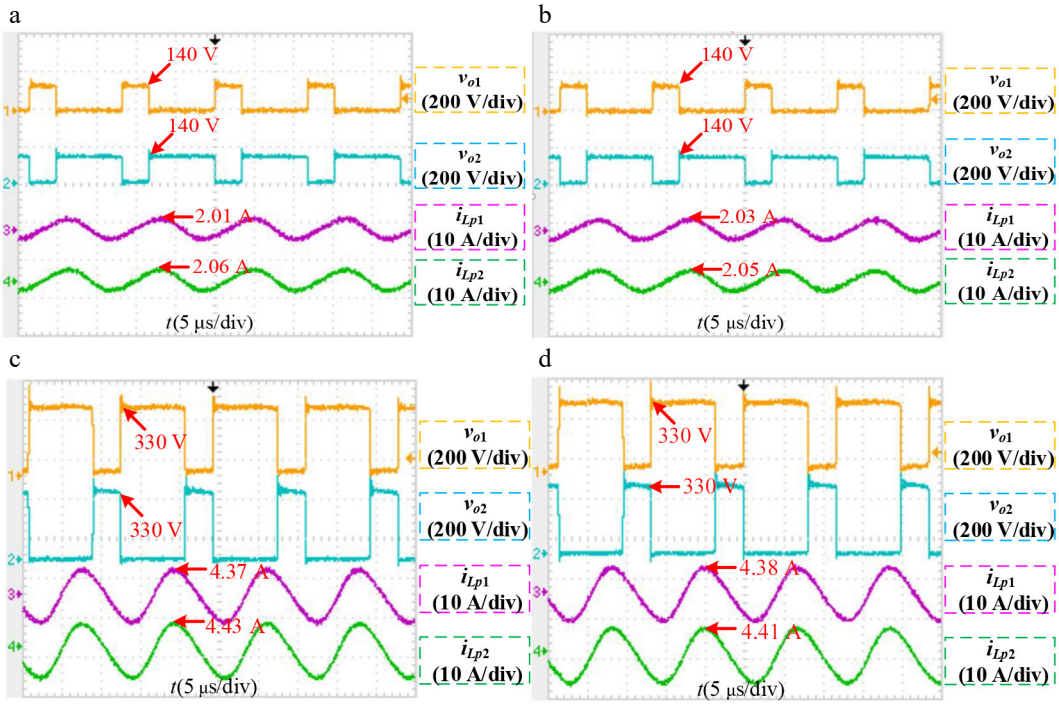

Fig. 15 Experimental waveforms of the inverter output voltages and primary coil currents. (a) $x = 0$, $D = 0.3$; (b) $x = 7.5$, $D = 0.3$; (c) $x = 0$, $D = 0.7$; (d) $x = 7.5$, $D = 0.7$.

increasing D, the effective values of rail current are approximately 2 and 4.4 A, respectively. Using Eqs (10) and (15), the inverter output voltage gains are calculated to be 0.534 and 1.175, verifying the voltage output capability of the dual-output inverter.

Figure 16 shows the switching waveforms of S_1 and S_2 at $x = 7.5$, $D = 0.3$; $x = 0$, $D = 0.3$; $x = 7.5$, $D = 0.7$; and $x = 0$, $D = 0.7$. v_{S1} and v_{S2} are the terminal voltages of S_1 and S_2 respectively. Taking $x = 7.5$ cm, $D = 0.3$ as an example: At t_0, S_1 is turned off and the drive voltage begins to decrease. At t_1, S_2 is turned on and the drive voltage starts to rise; prior to this, v_{S2} has dropped to zero, indicating that S_2 achieves ZVS turn-on. At t_2, S_2 is turned off and the drive voltage begins to decrease. At t_3, S_1 is turned on and the drive voltage begins to rise. Before that, v_{S1} has dropped to zero, indicating that S_1 achieves ZVS turn-on. Further analysis confirms that S_1 and S_2 achieve ZVS turn-on in all other waveforms. Combined with Figs. 11 and 14b, these results demonstrate that S_1 and S_2 can achieve ZVS turn-on under different duty cycles throughout the movement of the receiver coil from transmitting rail 1 to transmitting rail 2.

Figure 17 shows the characteristic curves of system output power P_{out} and efficiency η. It can be seen that P_{out} fluctuates to some extent as the receiving coil moves, with larger fluctuations occurring at higher D values. P_{out} reaches its maximum when the receiving coil is directly aligned with each transmitting rail ($x = -7.5$ cm and $x = 7.5$ cm). According to Eq. (16) and Fig. 9, when L_a and R are constant, P_{out} is positively correlated with $M_1 + M_2$ for a given D. As shown in Fig. 14, $M_1 + M_2$ and P_{out} reach their maximum values at $x = -7.5$ cm and $x = 7.5$ cm, which is consistent with the theoretical analysis. The efficiency curve shows that η also fluctuates with the movement of the receiving coil, and at the same x, η decreases slightly with increasing D. Overall, the system maintains high transmission efficiency across different x and D values, with a maximum efficiency exceeding 90%.

Dynamic characteristic test

Figure 18 shows the load change waveform of the system at $D = 0.5$ and $x = -7.5$ cm. It can be seen that when the load changes, all

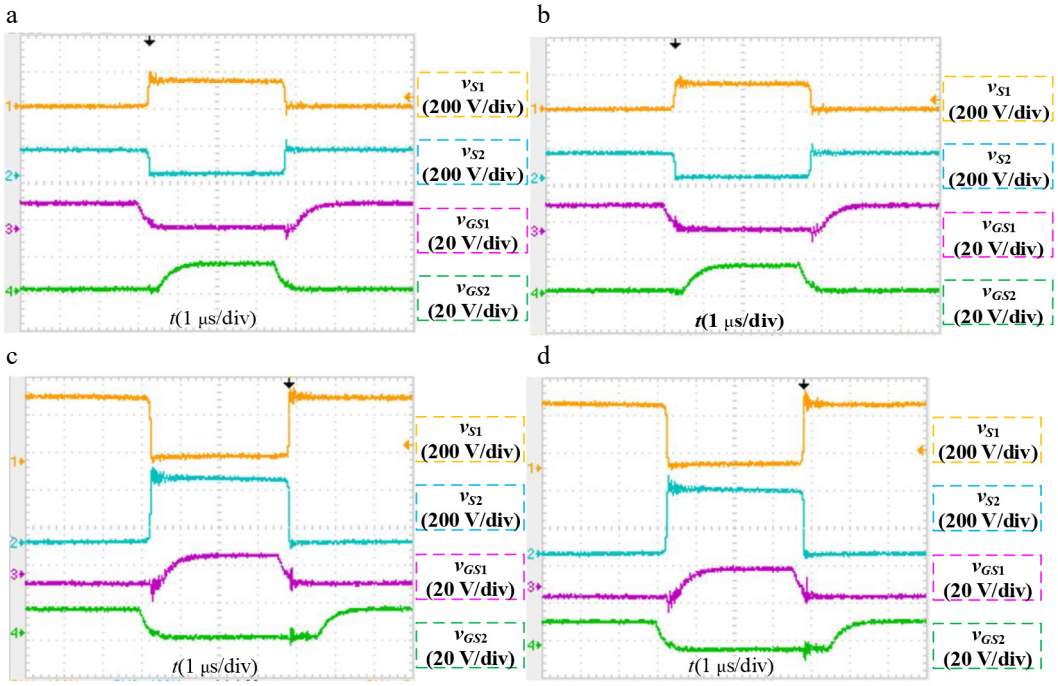

Fig. 16 Experimental waveforms of two switches. (a) $x = 7.5$, $D = 0.3$; (b) $x = 0$, $D = 0.3$; (c) $x = 7.5$, $D = 0.7$; (d) $x = 0$, $D = 0.7$.

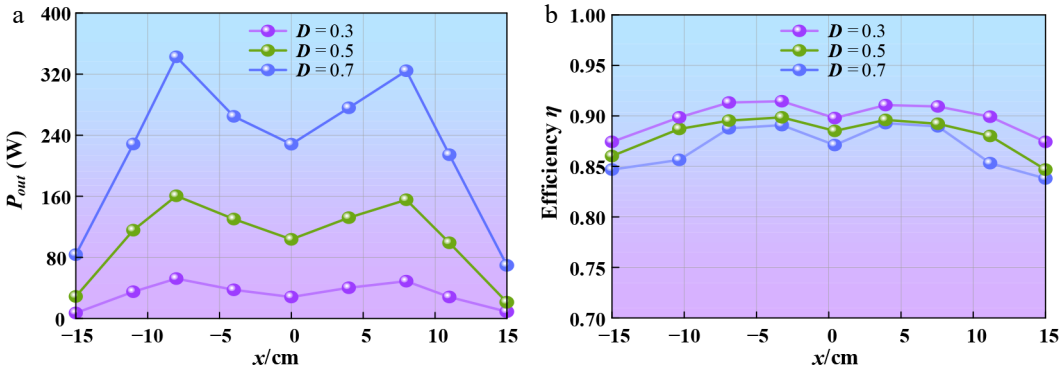

Fig. 17 Curves of the system output power and efficiency. (a) Output power; (b) Transfer efficiency.

parameters remain stable except for i_{L0}, which adjusts accordingly. The spike oscillation in V_{out} during load changes is attributed to the mechanical switch used to adjust the resistance, which introduces transient oscillations and noise during switching, affecting the V_{out} waveform. As observed, the system response time to load changes is only a few milliseconds, indicating a fast dynamic response.

Discussion

The proposed high-frequency dual-output inverter represents a significant advancement in the field of dynamic WPT for electric vehicles. By generating two identical output voltages to synchronously the transmitter coils, it effectively reduces the number of inverters and simplifies system control, addressing a long-standing challenge in multi-coil WPT systems. The wide output voltage gain range ensures sufficient voltage output capacity while minimizing the number of switches, reducing both hardware costs and overall system complexity. The ZVS feature of the inverter is another crucial advantage, as it significantly mitigates switching losses, thereby enhancing the overall efficiency of the WPT system.

The experimental results further validate the effectiveness of the proposed inverter. The WPT system demonstrates remarkable performance, maintaining high transmission efficiency across different positions of the receiver coil. With a maximum efficiency exceeding 90% and a minimum of around 85%, it outperforms many existing solutions. Additionally, the fast dynamic response speed ensures stable power transfer even under varying conditions. However, this research has limitations: the suppression of output power fluctuations, a critical issue in dynamic WPT systems, has not been fully addressed. Future research will focus on developing effective suppression technologies to enhance the stability of electric vehicle dynamic wireless charging systems, promoting the practical application and widespread adoption of this promising technology.

Conclusions

A high-frequency dual-output inverter with wide soft-switching range for dynamic WPT of electric vehicles is proposed. This inverter can generate two identical output voltages to realize the synchronous drive of the two transmitter coils, reducing the number of

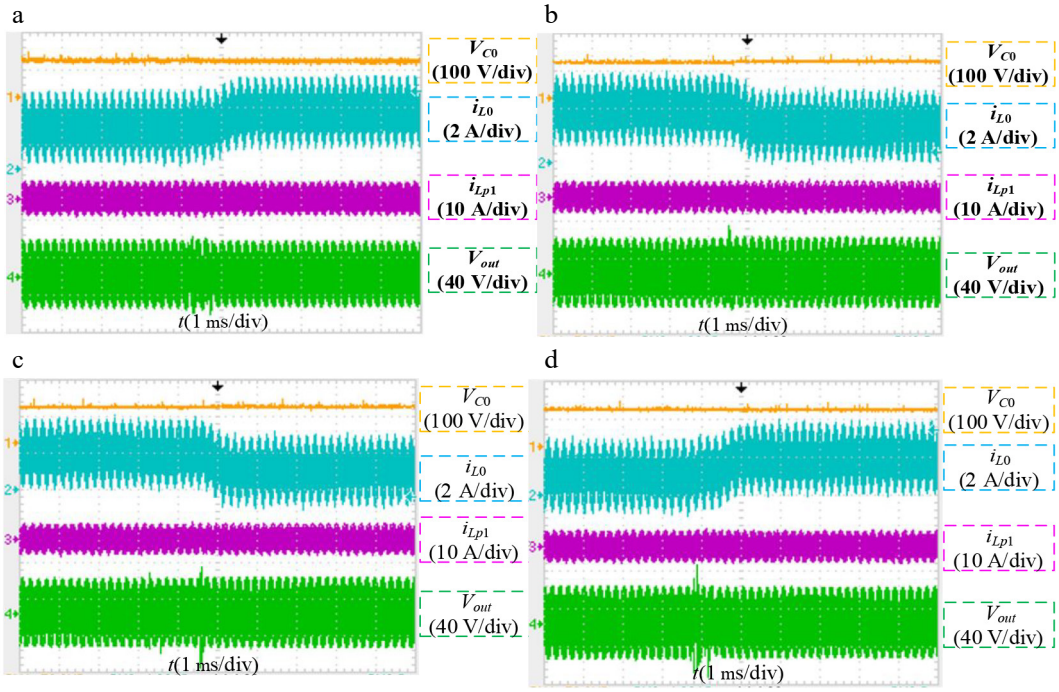

Fig. 18 Experimental waveforms of V_{C0}, i_{L0}, i_{Lp1}, and V_{out} under load change: (a) 5 to 3.3 Ω; (b) 3.3 to 5 Ω; (c) 5 to 10 Ω; (d) 10 to 5 Ω.

inverters and simplifying system control. The inverter's output voltage gain is [0, 1.39], which can guarantee the voltage output capacity with fewer switches compared with the existing inverters in WPT system, thus further reducing the number of switches required by the system. The switches can achieve zero-voltage soft-switching, minimizing switching losses. The experimental results show that the WPT system based on the proposed dual-output inverter can maintains high transmission efficiency across different positions of the receiving coil, with a maximum efficiency exceeding 90% and a minimum of approximately 85%. Moreover, the system exhibits a fast dynamic response speed.

Future research will focus on output power fluctuation suppression technologies for dynamic wireless charging systems in electric vehicles.

Author contributions

The authors confirm their contributions to the paper as follows: study conception and design: Wang R, He Y; data collection: Wang Y, He Y; analysis and interpretation of results: Wang R, Ding P, Zhu G, Mei Y; draft manuscript preparation: Wang R, Ma Z, Sun H, Li L. All authors reviewed the results and approved the final version of the manuscript.

Data availability

All data included in this study are available upon request from the corresponding author.

Acknowledgments

The National-level Innovation Training Program for College Students in Tianjin Municipality under Grant No. 202510058027.

Conflict of interest

The authors declare that they have no conflict of interest.

Dates

Received 30 June 2025; Revised 25 August 2025; Accepted 8 October 2025; Published online 15 January 2026

References

[1] Jo CH, Kim DH. 2025. Simplified integration of bidirectional OBC and WPT charging systems with reconfiguring topology for electric vehicles. *IEEE Transactions on Power Electronics* 40:7651–7656

[2] Farajizadeh F, Vilathgamuwa DM, Jayathurathnage P, Ledwich G. 2020. Graph sets method for multicoil wireless power transfer systems—Part I: principles. *IEEE Transactions on Power Electronics* 35:10741–10756

[3] Cheng C, Li W, Zhou Z, Deng Z, Mi C. 2020. A load-independent wireless power transfer system with multiple constant voltage outputs. *IEEE Transactions on Power Electronics* 35:3328–3331

[4] Zhao L, Zhang C, Ouyang Y, Xiao J, Hu H, et al. 2024. An integrated 6.78-MHz class Φ2 converter using bifurcation phenomenon of resonance between the isolation transformer. *IEEE Transactions on Power Electronics* 39:12003–12007

[5] Jiang L, Costinett D. 2019. A high-efficiency GaN-based single-stage 6.78 MHz transmitter for wireless power transfer applications. *IEEE Transactions on Power Electronics* 34:7677–7692

[6] Stein ALF, Kyaw PA, Sullivan CR. 2019. Wireless power transfer utilizing a high-*Q* self-resonant structure. *IEEE Transactions on Power Electronics* 34:6722–6735

[7] Liu X, Wang G. 2016. A novel wireless power transfer system with double intermediate resonant coils. *IEEE Transactions on Industrial Electronics* 63:2174–2180

[8] Wang Y, Liu H, Wheeler P, Wu F. 2024. Implementation and analysis of an efficient soft-switching battery wireless charger with re-configurable rectifier. *IEEE Transactions on Industrial Electronics* 71:4640–4651

[9] Li S, Deng Q, Li Z, Hu W. 2025. Control-oriented closed-loop identification and input design in a wireless power transfer system. *Wireless Power Transfer* 12:e007

[10] Thiagarajan K, Deepa T, Kolhe M. 2024. Optimized coil design and advanced neural network control for enhanced wireless power transfer in electric vehicles using Taylor-based Firefly and Dove Swarm Optimization. *Wireless Power Transfer* 11:e012

[11] Liu H, Wang Y, Yu H, Wu F, Wheeler P. 2023. A novel three-phase omnidirectional wireless power transfer system with zero-switching-loss inverter and cylindrical transmitter coil. *IEEE Transactions on Power Electronics* 38:10426–10441

[12] Li Z, Zhu C, Jiang J, Song K, Wei G. 2017. A 3-kW wireless power transfer system for sightseeing car supercapacitor charge. *IEEE Transactions on Power Electronics* 32:3301–3316

[13] Hu H, Georgakopoulos SV. 2017. Multiband and broadband wireless power transfer systems using the conformal strongly coupled magnetic resonance method. *IEEE Transactions on Industrial Electronics* 64:3595–3607

[14] Wang X, Leng M, Zhang X, Tian Q, Zhou X, et al. 2024. Multioutput wireless charger for drone swarms with reduced switch requirements and independent regulation capability. *IEEE Transactions on Industrial Electronics* 71:4883–4895

[15] Choi SY, Jeong SY, Lee ES, Gu BW, Lee SW, et al. 2015. Generalized models on self-decoupled dual pick-up coils for large lateral tolerance. *IEEE Transactions on Power Electronics* 30:6434–6445

[16] Madawala UK, Thrimawithana DJ. 2011. A bidirectional inductive power interface for electric vehicles in V2G systems. *IEEE Transactions on Industrial Electronics* 58:4789–4796

[17] Zhou S, Mi CC. 2016. Multi-paralleled LCC reactive power compensation networks and their tuning method for electric vehicle dynamic wireless charging. *IEEE Transactions on Industrial Electronics* 63:6546–6556

[18] Ko YD, Jang YJ. 2013. The optimal system design of the online electric vehicle utilizing wireless power transmission technology. *IEEE Transactions on Intelligent Transportation Systems* 14:1255–1265

[19] Vardani B, Tummuru NR. 2019. Bidirectional wireless power transfer using single phase matrix converter for electric vehicle application. *TENCON 2019 - 2019 IEEE Region 10 Conference (TENCON), Kochi, India, 17–20 October, 2019*. USA: IEEE. pp. 1523–1528 doi: 10.1109/tencon.2019.8929288

[20] Cheng C, Zhang Y, Zheng X, Hua W. 2025. A full-range soft-switching class-E inverter achieving quasi-constant voltage output. *IEEE Transactions on Power Electronics* 40:7663–7667

[21] Zheng K, Ren J, Zhong W. 2025. A soft-switching secondary-side control method without AC current detection for wireless power transfer systems. *IEEE Transactions on Power Electronics* 40:3785–3797

[22] Wang Q, Guo G, Wang Y, Chen J. 2021. An efficient three-phase resonant DC-link inverter with low energy consumption. *IEEE Transactions on Power Electronics* 36:702–715

[23] Chu E, Zhang X, Sun Q, Li S, Xiong H, et al. 2016. Three-phase double auxiliary resonant commutated pole inverter topology and analysis of its working principle. *IET Power Electronics* 9:1536–1545

[24] Liu H, He L, Cheng B. 2025. A powerless fractional-order WPT system with extended zero voltage switching region. *IEEE Transactions on Industrial Electronics* 72:3525–3533

[25] Abramovitz A, Zhao B, Smedley KM. 2016. High-gain single-stage boosting inverter for photovoltaic applications. *IEEE Transactions on Power Electronics* 31:3550–3558

[26] Sarnago H, Lucía Ó, Burdío JM. 2017. Interleaved resonant boost inverter featuring SiC module for high-performance induction heating. *IEEE Transactions on Power Electronics* 32:1018–1029

[27] Xia J, Li S, Li T, Dai W, Liu Z, et al. 2025. An efficiency optimization method for doubled-sided LCC compensated inductive power transfer systems based on circuit parameter matching. *IEEE Transactions on Power Electronics* 40:6260–6271

[28] Huang Z, Qin T, Li XL, Ding L, Iu HH, et al. 2024. Synthesis of inductive power transfer converters with dual immittance networks for inherent CC-to-CV charging profiles. *IEEE Transactions on Power Electronics* 39:7766–7777